ROYAL SOCIETY
OF CHEMISTRY

EDGE ARTICLE

Check for updates

All publication charges for this article
have been paid for by the Royal Society
of Chemistry

A photoprogrammable electronic nose with switchable selectivity for VOCs using MOF films†

Peng Qin,[a] Salih Okur,[a] Chun Li,[a] Abhinav Chandresh, [ID][a] Dragos Mutruc,[b]
Stefan Hecht [ID][bcd] and Lars Heinke [ID] *[a]

Advanced analytical applications require smart materials and sensor systems that are able to adapt or be configured to specific tasks. Based on reversible photochemistry in nanoporous materials, we present a sensor array with a selectivity that is reversibly controlled by light irradiation. The active material of the sensor array, or electronic nose (e-nose), is based on metal–organic frameworks (MOFs) with photoresponsive fluorinated azobenzene groups that can be optically switched between their *trans* and *cis* state. By irradiation with light of different wavelengths, the *trans–cis* ratio can be modulated. Here we use four *trans–cis* values as defined states and employ a four-channel quartz-crystal microbalance for gravimetrically monitoring the molecular uptake by the MOF films. We apply the photoprogrammable e-nose to the sensing of different volatile organic compounds (VOCs) and analyze the sensor array data with simple machine-learning algorithms. When the sensor array is in a state with all sensors either in the same *trans*- or *cis*-rich state, cross-sensitivity between the analytes occurs and the classification accuracy is not ideal. Remarkably, the VOC molecules between which the sensor array shows cross-sensitivity vary by switching the entire sensor array from *trans* to *cis*. By selectively programming the e-nose with light of different colors, each sensor exhibits a different isomer ratio and thus a different VOC affinity, based on the polarity difference between the *trans*- and *cis*-azobenzenes. In such photoprogrammed state, the cross-sensitivity is reduced and the selectivity is enhanced, so that the e-nose can perfectly identify the tested VOCs. This work demonstrates for the first time the potential of photoswitchable and thus optically configurable materials as active sensing material in an e-nose for intelligent molecular sensing. The concept is not limited to QCM-based azobenzene-MOF sensors and can also be applied to diverse sensing materials and photoswitches.

Introduction

Smart sensor systems are desired for various fields such as healthcare,[1] food safety,[2] environmental monitoring,[3] and the Internet of Things.[4] For example, they have promising applications in the field of robotics, where intelligent sensors enable robots with human-like senses and can distinguish various chemical stimuli.[5–10] An important class of analytes are volatile organic compounds (VOCs). Apart from the fact that many odor and flavor molecules are VOCs, VOC sensing is very important

for many indoor situations. For example, VOCs may be released from paints and glues and may present a health hazard. The health risk of VOCs strongly depends on the specific molecules. For instance, benzene is carcinogenic and toluene is less dangerous. Another example relates to *n*-hexane and cyclohexane, where the human-health-related recommended exposure limit for *n*-hexane is 50 ppm whereas it is 300 ppm for cyclohexane.[11] Therefore, the precise VOC identification is important. To avoid cross-sensitivity, causing the sensor system to respond similarly to different VOCs, arrays of sensors with different specificities are used. Such a sensor array is often referred to as electronic nose (e-nose). For the detection of VOCs, e-noses enable short response times and a fast detection, which make e-noses more practical than gas chromatography,[12,13] where often necessary sample pre-processing further hinders practical applications. The sensors of an ideal e-nose have a high sensitivity, good selectivity, fast response/recovery, and a high stability/repeatability. In order to meet these requirements, various forms of gas and VOC sensor systems, including metal oxide semiconductor devices,[14,15] chemical resistors,[16] field effect transistors,[14,17] electrochemical sensors,[18]

[a]*Karlsruhe Institute of Technology (KIT), Institute of Functional Interfaces (IFG), Hermann-von-Helmholtz-Platz 1, 76344 Eggenstein-Leopoldshafen, Germany. E-mail: Lars.Heinke@kit.edu*

[b]*Humboldt-Universität zu Berlin, Department of Chemistry & IRIS Adlershof, Brook-Taylor-Strasse 2, 12489 Berlin, Germany*

[c]*DWI – Leibniz Institute for Interactive Materials, Forckenbeckstr. 50, 52074 Aachen, Germany*

[d]*RWTH Aachen University, Institute of Technical and Macromolecular Chemistry, Worringer Weg 2, 52074 Aachen, Germany*

† Electronic supplementary information (ESI) available. See DOI: 10.1039/d1sc05249g

gas capacitance,[19] surface acoustic wave[2] and quartz crystal microbalances (QCM),[20,21] have been investigated and developed; see Table SI1 in the ESI† for comparison.

For an ideal sensor performance, the active sensing material should have a large specific surface area, resulting in high sensitivity, and a well-defined crystalline structure for high specificity. Nanoporous metal–organic frameworks (MOFs) fulfill these requirements. MOFs are formed by the self-assembly of metal nodes (*i.e.* ions or clusters) and organic ligand molecules connecting 2 or more metal nodes, resulting in scaffold-like materials.[22] The material has distinctive features such as a very high porosity, large specific surface area as well as structural and functional diversity.[23,24] The potential of MOFs as active sensor material has been demonstrated and explored in gravimetric, electric and optical sensing devices.[25–34] MOF sensors for gases and vapors with high sensitivity, high selectivity and low-power consumption were presented,[35] for example for the selective detection of NO_2 or ethanol.[36,37] Gravimetric transducers like MOF-coated QCM sensors, which are simple to prepare and have fast response and recovery characteristics, attract particular attention.[20] In a few studies,[21,34,38] QCM-based MOF sensor arrays have been prepared for the detection and discrimination of various molecules.

An important feature of MOFs is that their structure and properties can be designed to a wide extent by incorporating functional molecular components. In this way, MOF structures possessing light-responsive molecules such as azobenzene allow the remote control of adsorption and diffusion properties.[39–44] Sensor arrays (made of MOFs or other active materials) which can be remote-controlled by light and which have a photoprogrammable sensor performance have not yet been presented. Such a programmable e-nose should allow the controlled detection and classification of VOCs, depending on the respective condition.

Here, we present a remote-controllable e-nose system where the sensor performance, including its cross-sensitivity for detecting various VOCs, can be modulated and configured by light irradiation. It is based on an array of four QCM sensors coated with identical nanoporous photoswitchable MOF films. The MOF films are prepared directly on the QCM sensors in a layer-by-layer fashion, resulting in surface-mounted MOFs (SURMOFs).[45,46] The SURMOFs have a pillared-layer structure based on Cu-paddle-wheels. The MOF structure possesses azobenzene side groups, which can be switched between a *trans* and a *cis* state by light of the proper wavelength. The azobenzene groups are fluorinated at the ortho position, allowing the selective photoisomerization by exciting the n–π* transition. This enables the photoswitching with visibly light only, avoiding potentially harmful UV-light.[47,48] The MOF films have been previously presented with the aim of photoswitchable membrane separation and proton conduction.[42,49] The e-nose responses to four different VOC molecules were tested and the accuracy of classifying the VOCs was quantified by machine learning algorithms based on k-nearest neighbor (kNN)[50] analysis and linear discriminant analysis (LDA). The data show that the accuracy for classifying the VOCs is rather low when all

individual MOF films of the sensor array are switched to the same state, comprised of the same *trans–cis* ratio. In strong contrast, photoprogramming the sensor array to a state where each sensor has a different *cis–trans*-ratio results in a distinct response of each sensor. As a result, the specificity of the sensors in the array increases, the cross-sensitivity decreases, and the e-nose shows perfect classification accuracy for the studied VOCs. The study shows that the controlled isomerization in the nanoporous films allows to program the selectivity of the sensor array. The here presented concept based on reversible photochemistry in active sensing materials is neither limited to azobenzene as photoswitch, nor to MOFs as active sensing materials, nor to gravimetric transducer based on QCM. We believe this concept can be applied to various active materials in sensors combined with different transducer techniques and photoswitches.

Experimental section

Synthesis of SURMOF films

The SURMOF films with a $Cu_2(F_2AzoBDC)_2(dabco)$ structure were prepared in a layer-by-layer fashion on the substrates. F_2-AzoBDC stands for (*E*)-2-((2,6-difluorophenyl)diazenyl)terephthalic acid[42] and dabco for 1,4-diazabicyclo[2.2.2]octane. By using Accelrys/BIOVIA Material Studio, the accessible surface area of the $Cu_2(F_2AzoBDC)_2(dabco)$ structure was calculated to be approximately 740 m^2 g^{-1}, which is similar to comparable pillared-layer MOFs with side groups pendant to the linker.[51] The SURMOFs were synthesized by alternatively exposing the substrate to ethanolic $Cu(OAc)_2 \cdot H_2O$ solution (1 mM) and to ethanolic $F_2AzoBDC$ and dabco solution (each 0.1 mM). During the preparation, the substrates were sequentially immersed in the metal solution for 15 min, in pure ethanol for 2 × 1 min, in the linker solution for 30 min and again in pure ethanol for 2 × 1 min. The synthesis was performed with a dipping robot. The synthesis temperature was 50 °C. The sensor samples were prepared in 100 synthesis cycles, 20 cycles for the UV-vis experiments and 30 cycles for the infrared reflection absorption spectroscopy (IRRAS) experiments. Prior to the SURMOF synthesis, all QCM substrates (with a silver surface) and all IRRAS substrates (which are gold-coated silicon substrates) were functionalized with 11-mercapto-1-undecanol (MUD) self-assembled monolayers (SAMs). The quartz substrates for the UV-vis absorption measurements were functionalized by UV-ozone treatment before the SURMOF synthesis.

Sample characterization

The X-ray diffraction (XRD) analysis was performed using a Bruker D8-Advance diffractometer with a Bragg–Brentano (θ–θ) geometry (also referred to as out-of-plane) with a wavelength of λ = 0.154 nm. The (111) peak of the gold substrate is used as reference, verifying the correct sample height.

UV-vis transmission spectra were recorded with an Agilent Cary 5000 spectrometer and UMA unit.

Infrared spectral analysis was performed with a Fourier-Transform Infrared Reflection Absorption Spectrometer (FT-

IRRAS). The spectra were recorded with an incidence angle of 80° with respect to the normal.

Sensor array

The electronic nose is a home-built 4-channel QCM system, as sketched in Fig. 1b. Photographs of the setup are shown in the ESI, Fig. SI1.† Each quartz sensor has AT-cut and has a circular Ag top electrode with a diameter of about 4 mm and an area of 12.6 mm^2. This is the area covered by the SURMOF. The resonance frequency of the sensors is 10 MHz. The QCM sensors were obtained from JWT China. The frequency shift of the QCM sensors due to mass changes are recorded every 1–1.7 s. The entire electronic nose system was controlled by a program code written in MATLAB. Previous versions of the home-built sensor arrays are described in ref. 21, 38 and 52.

The gas atmosphere inside the electronic nose cell was controlled by two mass flow controllers (MFCs), see Fig. 1b. The gas stream of the carrier gas (nitrogen) was divided into 2 streams, one stream provides a constant nitrogen flow of 300 ml min^{-1} for the desorption process. The other stream passes through the liquid VOC-filled wash bottle to produce a VOC-enriched vapor stream with a vapor pressure somewhat smaller than the saturation vapor pressure, see ESI.† It can be instantly switched between both gas streams.

Each sensing experiment was composed of 3 phases. First, the sensor was exposed to pure nitrogen, this means potential guest molecules desorb and the MOF pores are emptied. This results in a stable baseline. Then, the vapor of the VOC molecules passes through the cell with the sensor array. The VOCs adsorb in the SURMOF, causing a mass increase and a frequency shift in the QCM sensor. The third step is the

desorption of the adsorbed VOCs in a pure nitrogen atmosphere. The adsorption step is 1 h and the desorption step is usually 8 h to ensure that all VOC molecules are desorbed. All experiments were performed at room temperature.

For photo-programming the sensor array, the SURMOF samples were irradiated with light of 400 nm, 450 nm, and 530 nm wavelength. For this, LEDs from Prizmatix with 65, 60, and 55 mW power, respectively, were used, which corresponds to light intensities of about 3 mW cm^{-2}. The irradiation time was 15 min. This time is longer than the time required for realizing the equilibrium state under similar conditions in previous studies, typically 5 to 10 min,[42,49] so the photostationary state (PSS) should be reached. Before irradiating the sensor with different wavelengths, the sensors were thermally relaxed at 70 °C in a nitrogen atmosphere for 3 days. This ensures that the sample was in the thermodynamically-stable 100%-*trans* state. Please note, the samples were irradiated before the sensing experiments and all the sensing experiments were performed in the dark, where the *trans–cis* ratio is stable during the course of the experiments.[47,48]

Data analysis

Data analysis and classification were performed using standard k-nearest neighbor (kNN) machine learning algorithms *via* a program code written in *Python*.[50,53] For the kNN classification, a total of 100 data points were collected before the end of the vapor exposure period, this means when the equilibrium is (essentially) reached. With the sampling rate of the device, this corresponds to a time period of approximately 2.5 min (*i.e.* approximately 57.5 min to 60 min after the beginning of the VOC exposure). Each data point includes the signals of all four sensors, thus each data point is a 4-dimensional vector. A total of 400 data points were collected for the 4 odors. The K value in kNN was set to 20 (corresponding to the square root of the number of data points, which is recommended as reasonable value for K (ref. 54–56)). Data were classified using 10-fold cross-validation, where 90% of the data points (*i.e.*, 360 points) were used as the training set and 10% were used as the test set (40 points). The outcome of the kNN algorithm is the grouping of the data to the different classes (*i.e.* the vectors of the test set are grouped according to the smallest distances of the vectors to each other) and the comparison if the assignments to the classes were correct or wrong, shown in the confusion matrix. The file with the program code is also uploaded. In addition, we performed linear discriminant analyses (LDA) of the data.
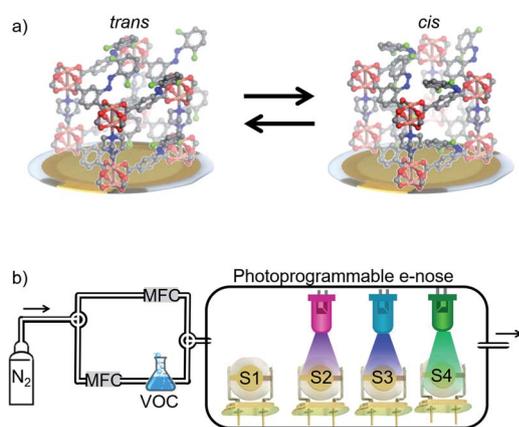
Results and discussion

The structure of the Cu-paddle-wheel-based pillared-layer SURMOF is sketched in Fig. 1, where dabco is the pillar molecule and the layer linker molecule (F$_2$AzoBDC) possesses a fluorinated azobenzene side group. The SURMOF films were prepared in a layer-by-layer fashion. The number of synthesis cycles, which is 100, was chosen as trade-off between a good signal-to-noise ratio (improved by thicker films with more total uptake) and slow uptake rates (caused by thick films, where the

Fig. 1 (a) The structure of Cu$_2$(F$_2$AzoBDC)$_2$(dabco) SURMOF on a QCM sensor. The azobenzene side groups of the SURMOF can isomerize from the *trans* form (left-hand side) to the *cis* form (right-hand side) and *vice versa*. Carbon atoms are shown in gray, oxygen in red, copper in orange, fluorine in green, and nitrogen in blue. Hydrogen atoms have been omitted. (b) Sketch of the sensor array setup. The nitrogen gas flow is split into two streams, which fluxes are controlled by mass flow controllers (MFCs). One nitrogen stream is enriched with the VOC vapor by bubbling through a wash bottle. The photoprogrammable e-nose comprises four SURMOF-coated QCM sensors (S1, S2, S3, and S4) that can be selectively irradiated in the cell.

uptake time roughly scales with the square of the film thickness).

The X-ray diffractograms of all samples, Fig. 2a, are very similar. The observed diffraction peaks agree with the reflexes calculated for $Cu_2(F_2AzoBDC)_2(dabco)$ MOF, showing that the SURMOFs have the targeted structure. Moreover, the fact that only the (001) and (002) can be observed in the out-of-plane geometry indicates that the SURMOFs are grown in the (001) orientation perpendicular to the substrate surface. The

Fig. 2 (a) X-ray diffractograms (XRDs) of $Cu_2(F_2AzoBDC)_2(dabco)$ SURMOF films on the QCM sensors. As reference, the calculated XRD of the targeted structure is shown in grey. The sensors and the experimentally observed diffraction peaks are labeled. (b) UV-vis absorbance spectra and (c) IRRA spectra of the $Cu_2(F_2AzoBDC)_2(-dabco)$ SURMOF. The thermally-relaxed sample (100% *trans*) is labeled as dark (black). The sample upon irradiation with violet, blue and green light are shown in violet, blue and green. In panel (b) and (c), zoom-ins of the n−π*-bands and of a *trans*-azobenzene-vibration band at 957 cm^{-1}, respectively, are shown.

diffractogram of a $Cu_2(F_2AzoBDC)_2(dabco)$ MOF in the form of a powder is shown in ref. 57.

The photoisomerization of the samples upon irradiation with green (530 nm), blue (450 nm) and violet (400 nm) light was explored by UV-vis and infrared reflectance absorption spectroscopy (IRRAS), Fig. 2b and c. The UV-vis spectra show that the thermally relaxed sample exhibits a strong π−π*-absorption band at 320 nm. Upon violet light irradiation, the π−π* band at 320 nm is slightly reduced with respect to the thermally relaxed samples, while irradiations with blue or green light lead to a significant reduction of the π−π* band. In addition, the n−π* band at about 450 nm was shifted to a smaller wavelength by green light irradiation, while the subsequent blue and violet light irradiation shifted the n−π* band to a larger wavelength. The UV-vis spectra are a clear indication that the azobenzene side groups in the MOF can be switched from *trans* to *cis* and *vice versa* by irradiation with light of specific wavelengths. The light-response of the UV-vis spectra, which is in agreement with spectra obtained for fluorinated azobenzene in solution,[47] indicates that the photostationary state (PSS) upon violet light irradiation results in a *trans*-rich mixture (with only a small fraction of *cis* molecules), green light results in a *cis*-rich mixture, and blue light results in a mixed *trans*/*cis* state. The *trans*–*cis* isomerization presumably takes place *via* rotation, Fig. SI11.†

To quantify the photoisomerization yield and to characterize the PSS, IRRAS measurements were performed, Fig. 2c and SI3.† To this end, the area of the *trans*-azobenzene vibration band at 957 cm^{-1} was analyzed.[42,57] While all azobenzene groups in the thermally relaxed sample are in the *trans* state (and 0% is in *cis*), the percentage of *trans* azobenzene is reduced upon light irradiation. Upon violet light, 86% of the azobenzene moieties are in the *trans* state (and 14% *cis*). Upon blue light irradiation, 53% of the azobenzene are in *trans* (and 47% *cis*). Green light irradiation results in 14% *trans* and 86% *cis*. These switching yields are consistent with previous studies.[42,57] It should be noted that, in the dark, the *cis* isomers transform to thermally-relaxed *trans* isomers with a time constant of up to 2 years at room temperature.[47,48] Thus, the isomer ratio is constant during the course of the experiments, unless the SURMOF is irradiated by light.

For the photoprogrammable e-nose, four QCM sensors were coated with $Cu_2(F_2AzoBDC)_2(dabco)$ SURMOF thin films. The XRDs of the samples, shown in Fig. 2a, show that all 4 samples have a very similar crystallinity and all four samples are grown in an oriented fashion. This means the samples are grown in (001) orientation perpendicular to the substrate, as shown in Fig. 1a.

The scanning electron microscopy (SEM) images, Fig. SI2† in the ESI,† show all samples are homogenous. The MOF films are composed of small crystallites of about 0.25 μm extension. The top view images show that there are no visible differences between the different sensors. The thickness of the MOF film is approximately 0.2 μm.

To explore the controllable selectivity of the e-nose, the gas adsorption characteristics of the sensor array were investigated for the exposure to different VOCs. From the large class of VOCs, we chose four representatives, which are rather small allowing
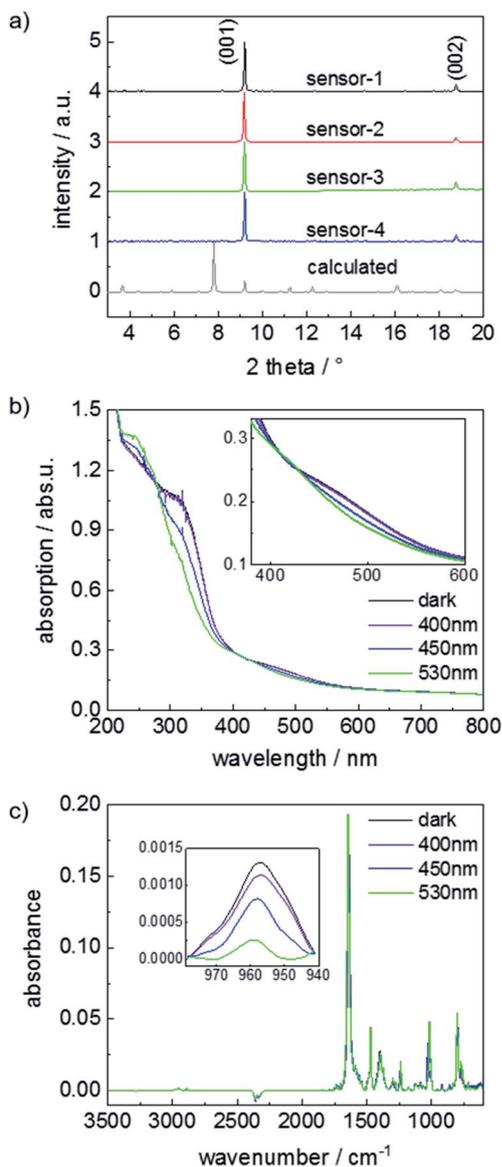
for a fast mass transfer (*i.e.* a relatively fast sensors response) and show different molecular features like polarity, thus different molecular (in particular polar) interactions. To this end, 1-propanol, 1-butanol, *n*-hexane and cyclohexane were chosen. Initially, the QCM sensor array is in a nitrogen stream. Then, the e-nose is exposed to the VOCs by instantly switching from the pure nitrogen stream to the carrier gas enriched with the pure VOC vapor. The sensor frequency shifts, which are proportional to the mass change of the film caused by the guest uptake, are recorded. These frequency shifts are used as the signal of the sensor, as shown in Fig. 3. Experiments with the blank QCM sensor (without SURMOF coating, Fig. SI4†) were performed, showing no response to the VOCs or to light irradiation.

The responses of the array with all SURMOF sensors in the 100%-*trans*/0%-*cis*-state to the exposure to the vapor of 1-propanol and cyclohexane are shown in Fig. 3a and d. The corresponding responses of the array to 1-butanol and *n*-hexane are shown in Fig. SI4 in the ESI.† The signals of all four sensors as response to the respective VOCs are essentially identical. This is expected since all four samples are SURMOFs with identical structures and similar thicknesses and properties, although small deviations, potentially caused by different defect

densities, cannot be prevented. The sensor data as response to the VOC exposure with the entire array in the 86%-*cis*-state are shown in Fig. 3b and e and SI4.† All sensors show again the same results for the respective VOC, but with slightly different frequency shifts compared to the all-*trans*-array.

The sensor responses of the array where each sensor is selectively irradiated so that each sensor has a different *trans*–*cis* ratio are shown in Fig. 3c and f and SI4.† Then, the different sensors show different responses to 1-propanol and 1-butanol.

The final signal, after about 1 h of exposure to the VOC vapor, is used for further evaluation. Fig. 4a shows the radar plots of the frequency shifts of the responses to different VOCs without and with photoprogramming. For the e-nose when all samples
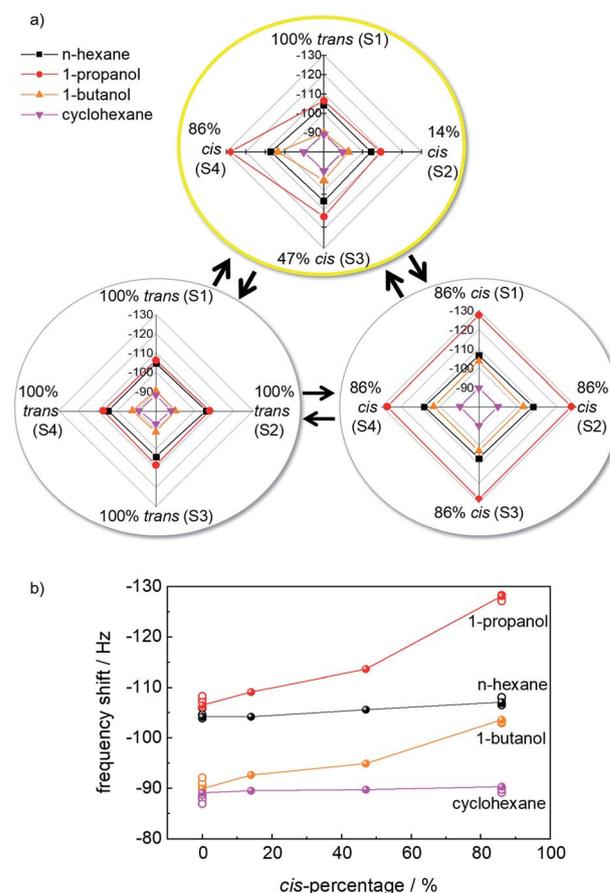
Fig. 4 (a) Radar plot of the sensor array data for the different VOCs. The 2 radar plots at the bottom are obtained after switching all the SURMOF films to the 100%-*trans*-state (left-hand side) or to the 86%-*cis* state (right-hand side). The radar plot on the top (yellow circle) is obtained after selectively switching each sensor to a different state, *i.e.* with 0%, 14%, 47% and 86% *cis* isomers. The axes are the recorded frequency shifts of the sensor for the respective VOC. All axes of the radar plots have the same scale (from −80 to −130 Hz). The VOCs are 1-propanol (red), *n*-hexane (black), 1-butanol (orange) and cyclohexane (magenta). (b) Frequency shift *versus* the percentage of *cis*-azobenzene in the SURMOF sensors. The solid spheres connected by solid lines are the data from the photoprogrammed e-nose (yellow top-radar plot in panel (a)). The all-sensor-in-100%-*trans* and −86%-*cis* data are shown as open symbols. The frequency scale of all plots (a and b) is from −80 Hz to −130 Hz.
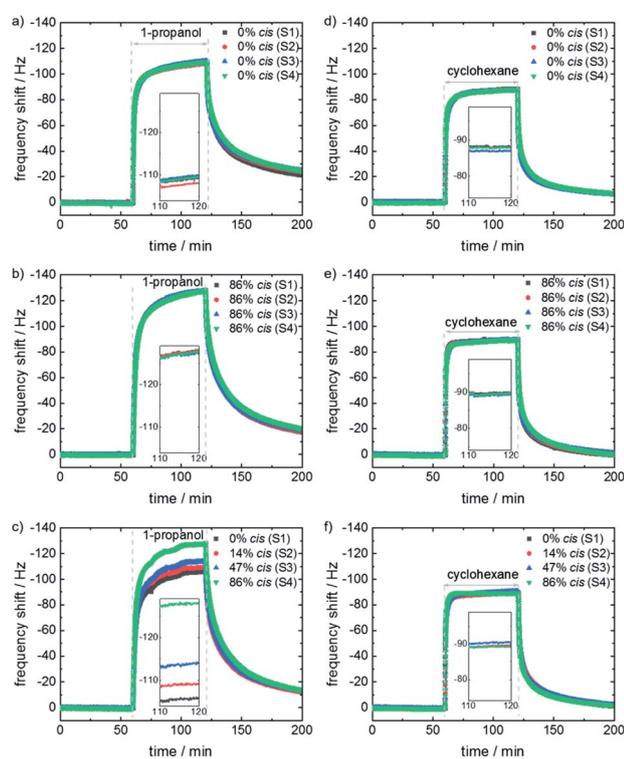

Fig. 3 E-nose response to the exposure to 1-propanol (a–c) and cyclohexane (d–f) vapor as a function of time. All azobenzene-groups in the sensor array are in the 100%-*trans* state in (a) and (d) and in the 86%-*cis*-state in (b) and (e). In panel (c) and (f), the sensor array is photoprogrammed such that the azobenzene groups are in 100%-*trans* (0%-*cis*) in sensor 1 (S1), 14%-*cis* in sensor 2 (S2), 47%-*cis* in sensor 3 (S3) and 86%-*cis* in sensor 4 (S4). For comparison, all plots have the same scale. The insets show zoom-ins of the data at the end of the analyte exposure where the *y*-scale is 25 Hz.

are in the 100%-*trans*-state or in the 86%-*cis*-state, all sensors show essentially identical responses. For the 100%-*trans*-array, the signal for 1-propanol and *n*-hexane as well as 1-butanol and cyclohexane are very similar. As a result, their discrimination by the sensor array is not possible.

The situation changes when the sensor array is irradiated selectively with violet, blue and green light. The sensor responses to the VOCs 1-propanol and 1-butanol vary for the different sensors. The radar plots, Fig. 4a, show that the responses of the VOCs are different and each VOC shows a specific pattern. This means the absolute values of the frequency shifts and their ratios to each other are unique for each VOC analyte. The different VOC molecules can be principally distinguished by their patterns in the radar plots.

Fig. 4b shows the relationship between the sensor response to the VOCs *versus* the percentage of *cis*-azobenzene in the SURMOF sensors. The data show that for polar molecules (here: 1-propanol and 1-butanol) the uptake amount increases with increasing *cis*-azobenzene content. On the other hand, the uptake by the MOF films is essentially not affected by the *cis*-ratio for non-polar molecules (here: *n*-hexane and cyclohexane). These data indicate that the signal changes upon photo-isomerization can be explained by the changes of the molecular dipole moment of azobenzene. While *trans*-azobenzene is a non-polar molecule, the dipole moment of the *cis* isomer is 3 Debye.[42] The increased polar character of the MOF material as result of the *trans*-to-*cis* isomerization causes the increased uptake amount of polar molecules.

Generally, the interactions between the targeted VOC analytes and the MOF host are primarily based on polar interactions, such as hydrogen bonding and dipole–dipole interactions. Moreover, halogen bonding, OH–π, CH–π, dispersion and non-polar interactions may contribute.[58–60] In a previous study,[49] quantum chemical calculations of a diol in the pores of this MOF structure showed that a hydrogen bond forms between the nitrogen atoms of the azobenzene in the *cis* form and the OH group of the guest molecule. On the other hand, the calculations also showed that there is no strong interaction when the azobenzene is in the *trans* form. Thus, we conclude that the *trans*–*cis*-adsorption-switching effect, and hence the basis for the signal photoprogramming, is based on the hydrogen-bond formation between the polar analytes and the *cis*-azobenzene, whose amount is tuned by light. In line with this finding, the signals of the nonpolar analytes are hardly affected by the photoprogramming. The result that the polar interaction, rather than steric effects of the azobenzene switching, dominates the adsorption properties was also found in similar azobenzene-containing MOFs.[61,62]

In order to quantify the sensor performance, the sensor array data were analyzed with a k-nearest neighbor (kNN) machine learning algorithm. The confusion matrixes, Fig. 5 and SI6,† are visual representations of the classification results for the test data. The correct classification of the VOC molecules is shown in green on the diagonal of the confusion matrix and the wrong classification is shown in red. The confusion matrix for the array with all sensors in 100%-*trans*-states is shown in Fig. 5a. The average accuracy is only 46% and it is not possible to
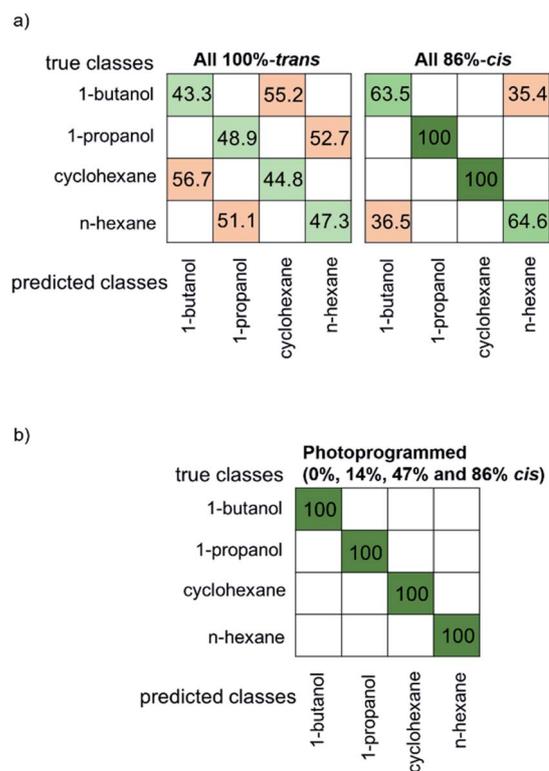

Fig. 5 Confusion matrixes for the classification of 4 molecules by kNN. (a) The sensor array is in the all-100%-*trans* state (left) and in the all-86%-*cis*-state (right). The average accuracy for all 4 VOCs is 46% for all-100%-*trans*-state and 82% for all-86%-*cis*-state. (b) The sensor array is programmed by light irradiation so that one sensor is in the 100%-*trans*-state, one in 14% *cis*, one in 47% *cis* and one in 86% *cis*. The sensor array shows perfect classification accuracy, *i.e.* 100%, without any misclassification.

reliably distinguish between different VOC molecules. Please note, a total random classification of the 4 VOCs would result in an accuracy of 25%. Here, severe cross-sensitivity occurs between 1-butanol and cyclohexane as well as between 1-propanol and *n*-hexane. A slightly better, but still not ideal sensor performance is found for the array with all sensors in the 86%-*cis* state, Fig. 5a, where an average accuracy of 82% was found.

Remarkably, the cross-sensitivity between the sensor array in all-*trans* and all-86%-*cis*-state changes. While 1-butanol and cyclohexane cannot be distinguished by the sensor array in the all-*trans*-state, these two molecules can be perfectly discriminated by the all-86%-*cis* array. However, the all-86%-*cis*-array cannot distinguish 1-butanol and *n*-hexane, which, on the other hand, can be perfectly distinguished by the all-*trans*-state-array.

The confusion matrix for the e-nose upon selectively photoprogramming the sensors of the array is shown in Fig. 5b. There, all VOCs can be identified and distinguished. The high classification accuracy is enabled by the individual MOF sensors which have (slightly) different adsorption properties, programmed by light. Thus, each sensor has a light-induced specificity, resulting in the prevention of cross-sensitivity.

The results of the analysis of the sensor data by linear discriminant analysis (LDA) are shown in Fig. SI5.† There, classification accuracies similar to the values determined by kNN were found.

The time course of the sensor signal, see Fig. 3, is determined by the uptake kinetics of the analytes by the MOF films. Generally, the molecular uptake by MOFs is controlled by intracrystalline diffusion, where the uptake time is proportional to the square of the film thickness.[63] In addition, further mass transfer resistances like surface barriers, hindering the molecules in entering the pore system and thus decelerating the uptake kinetics, can contribute or even dominate the uptake kinetics.[63–65] The uptake time constants determined with a mono-exponential function describing the uptake in the 100%-*trans*-MOF films are approximately 8 min, 5 min, 3 min and 6 min for 1-butanol, 1-propanol, cyclohexane and *n*-hexane, respectively. The final uptake is reached approximately 10 min to 40 min after starting the analyte exposure. There is only a very small variation between the different samples. While the observed uptake time constants are very similar for the MOFs in the *trans* and *cis* state for cyclohexane and *n*-hexane, the uptake rate decreases by a factor of about 2 for 1-butanol. For practical applications, the response time needs to be reduced, for instance by faster uptake in MOF films with larger pore diameters.

In addition to using the (final) equilibrium data for the analysis as done in Fig. 4 and 5, the transient sensor data can also be used to discriminate the molecules before the equilibrium state is reached. In Fig. 6, the discrimination accuracy of the sensor data *versus* time is shown. The data show that the sensor array reaches the final classification accuracy after about 10 min upon start of the analyte exposure. This means, the programmed sensor array shows sufficiently different signals allowing the reliable classification. It should be stressed that the sensor array reaches the final classification accuracy, although the uptakes are not yet in equilibrium at that time.
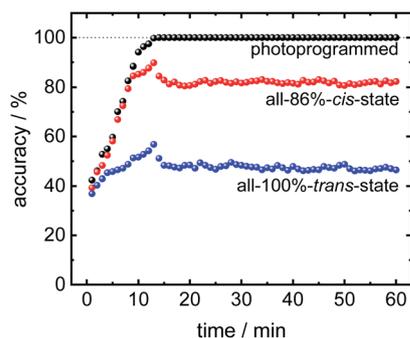
An important feature of the photoprogrammable e-nose is that the sensor performance only depends on the percentages of the isomerizations. Since the irradiation time is significantly longer than the time required for the photoisomerization, the PSS is reached, regardless of the initial state. An example is shown in Fig. SI6,† where the e-nose is selectively photoprogrammed with the same wavelengths but in a different order compared to the data in Fig. 3c, f and 5b. This means the sensor array was irradiated with violet, blue and green light and one sample is kept in the 100%-*trans*-state, however, the order of the sensors is opposite to the array-programming above. There, the obtained classification accuracy is again 100%. The data in Fig. SI6† show that the sensor response depends only on the *cis–trans* isomer ratio, *i.e.* on the irradiation, rather than on the specific sensor.

Here, we focused on four sensor states with defined *trans–cis* ratios, as a result of three different illumination wavelengths and thermal relaxation. More states with different *trans–cis* ratios can be realized by more light colors (*e.g.* with wavelengths between 400 nm and 530 nm) or by mixing the green and violet light, see *e.g.* ref. 66.

For practical sensor applications, regeneration and reproducibility are important features. By repeating the sensing experiments for 3 cycles, the reproducibility was explored, Fig. SI7.† The results of the individual cycles are very similar with standard deviations of less than 1 Hz. This is significantly smaller than the signal differences caused by the photoprogramming, see Fig. 4, indicating a high reproducibility of the sensor performance. The stability during a course of up to one month is explored in Fig. SI8 and SI9.† During that time period, the sensor performance is very similar, indicating a good long-term stability of the sensor, when stored in dry atmosphere. Based on the structural similarities to $Cu_2(BDC)_2(dabco)$, we assume that the carboxylate bonds break under the exposure to water and the MOF material degrades.[67] Good stability also in humid environment could be realized with similar azobenzene-containing, water-stable MOF structures, *e.g.* based on UiO-66.[68] The switching and the photoprogramming of the sensor performance to classify VOCs in humid environment and common air, as well as to classify VOC mixtures will be explored in the future.

The gravimetric sensing setup based on QCM possesses the advantage that a homogeneous, defect- and pinhole-free MOF film is not required. Defects, such as common surface barriers in MOFs, decelerate the uptake and release kinetics,[63,64] and thus slow down the sensor response, but do not hamper the sensitivity. We like to stress that these MOF films can be prepared as pinhole-free membranes,[42] thus they are also suited for other sensing techniques where crack-free sensor coatings are required or are at least very beneficial, like in transducer techniques based on impedance spectroscopy.[69]

Such photoswitchable MOF-films, where the guest affinity and guest–host interaction can be configured, can also be used with different transducer techniques, in particular in sensor setups where MOFs have proven to show very good sensor performance. For instance, in sensors based on electrochemical impedance spectroscopy in combination with substrates with

Fig. 6 The accuracy for the discrimination of the 4 analyte molecules at different time intervals. Each value is determined from 40 consecutive data points, corresponding to approximately a time interval of 1 min, where the final data points end at the values shown on the *x*-axis. The data of the all-100%-*trans*-MOF-array are shown in blue, of the all-86%-*cis*-MOF-array in red and the data of the photoprogrammed array (0%, 14%, 47% and 86% *cis*) are shown in black. The *x*-axis is the time after starting the exposure to the analytes.

deposited electrodes,[70] on field-effect-transistors,[71,72] on surface-acoustic-wave sensor[73] and also optical sensors.[27,74]

By using QCM sensors as transducer technique, the power consumption is significantly smaller than in other commonly used VOC sensing techniques, like using oxides working at higher temperature.[75,76] The power consumption of the photo-programmable MOF sensor can be further reduced by using different transducer techniques, *e.g.* based on impedance measurement or surface-acoustic wave sensors.[69,76,77] QCM-based sensor arrays can be rather small, so that they can be used as portable e-noses.

Conclusions

A QCM-based sensor array consisting of a photoresponsive nanoporous metal–organic framework as the active sensing layer has been presented. The metal–organic framework structure contains fluorinated azobenzene side groups, whose *trans–cis* isomerization can be tuned by light irradiation over a wide range, resulting in the modification of the adsorption properties. By selectively irradiating the MOF films, the sensor performance can be programmed by light. The performance of the 4-channel e-nose was explored for detecting and classifying the vapors of VOC analytes. While the discrimination accuracy for the e-nose with the sensors in the same state is rather low, ideal discrimination accuracy is reached for selectively switching the sensors, resulting in an array with high specificity and perfect sensor performance. Taking advantage of light to remotely control the properties of the individual sensors allows to reversibly program the sensor array performance.

We are convinced that such photoprogrammable active sensing materials can also be applied in other sensor setups, in particular in applications where MOFs are already found.[23,24,78,79] While the focus of our work has been on azobenzenes, the concept can also be applied to MOF films with other photoresponsive groups such as spiropyrans,[80,81] diarylethenes[82,83] or fulgides.[84] In addition to reversible photoisomerization, irreversible light-induced processes in MOFs can also be used.[85,86] Moreover, by using photoresponsive chiral MOF films, the realization of photoprogrammable enantioselective e-noses should be possible.[57,87] We are also convinced that the concept of photoprogrammable sensor arrays can be applied to other classes of active sensing materials. In particular, zeolites,[88] covalent-organic frameworks (COFs) and porous organic polymers,[89,90] mesoporous silicates[91,92] as well as metal and oxide nanoparticles,[93,94] which can also be functionalized with various photoresponsive molecules but also find applications in sensors, can be used. These materials are used in gravimetric transducers[95] and can also be used in different sensor setups.[35,96] Thus, there should be an enormous potential for photoprogrammable sensor arrays in target-specific smart sensing devices.

Data availability

The data is uploaded as ESI.†

Author contributions

PQ, supported by SO, performed the experiments and analyzed the data. CL prepared the MOF films. AC measured the SEM images. DM and SH synthesised the custom-made MOF linker. LH designed the project. PQ and LH wrote the manuscript, approved by all authors.

Conflicts of interest

There are no conflicts to declare.

Acknowledgements

Notes and references

1 R. Feiner, L. Engel, S. Fleischer, M. Malki, I. Gal, A. Shapira, Y. Shacham-Diamand and T. Dvir, *Nat. Mater.*, 2016, **15**, 679–685.

2 G. Ok, H. J. Kim, H. S. Chun and S.-W. Choi, *Food Control*, 2014, **42**, 284–289.

3 J. K. Hart and K. Martinez, *Earth-Sci. Rev.*, 2006, **78**, 177–191.

4 Z. P. Peng, *Adv. Mater. Res.*, 2014, **989–994**, 5520–5523.

5 S. Coradeschi, *IEEE Intell. Syst.*, 2006, **06**, 1541–1672.

6 M. Segev-Bar, N. Bachar, Y. Wolf, B. Ukrainsky, L. Sarraf and H. Haick, *Adv. Mater. Technol.*, 2017, **2**, 1600206.

7 Y. Liu, K. He, G. Chen, W. R. Leow and X. Chen, *Chem. Rev.*, 2017, **117**, 12893–12941.

8 Y. H. Jung, B. Park, J. U. Kim and T. I. Kim, *Adv. Mater.*, 2019, **31**, e1803637.

9 J. C. Yang, J. Mun, S. Y. Kwon, S. Park, Z. Bao and S. Park, *Adv. Mater.*, 2019, **31**, e1904765.

10 A. Chortos, J. Liu and Z. Bao, *Nat. Mater.*, 2016, **15**, 937–950.

11 National Institute for Occpational Safety and Health, *NIOSH Pocket Guide to Chemical Hazards*, 2007, NIOSH Publication No. 2005-149.

12 A. N. Baghani, R. Rostami, H. Arfaeinia, S. Hazrati, M. Fazlzadeh and M. Delikhoon, *Ecotoxicol. Environ. Saf.*, 2018, **159**, 102–108.

13 O. Kniemeyer, T. Fischer, H. Wilkes, F. O. Glockner and F. Widdel, *Appl. Environ. Microbiol.*, 2003, **69**, 760–768.

14 K. Natori, *J. Appl. Phys.*, 1994, **76**, 4879–4890.

15 S. Benedetti, S. Mannino, A. G. Sabatini and G. L. Marcazzan, *Apidologie*, 2004, **35**, 397–402.

16 F. Wang, Y. Yang and T. M. Swager, *Angew. Chem., Int. Ed.*, 2008, **47**, 8394–8396.

17 B. Wang, T. P. Huynh, W. Wu, N. Hayek, T. T. Do, J. C. Cancilla, J. S. Torrecilla, M. M. Nahid, J. M. Colwell, O. M. Gazit, S. R. Puniredd, C. R. McNeill, P. Sonar and H. Haick, *Adv. Mater.*, 2016, **28**, 4012–4018.

18 W. Wojnowski, T. Majchrzak, T. Dymerski, J. Gebicki and J. Namiesnik, *Sensors*, 2017, **17**, 2715.

19 D. E. J. Steven, M. Drew, C. E. Buss, K. M. D. D. I. MacEwan and K. R. Mann, *J. Am. Chem. Soc.*, 2001, **123**, 8414–8415.

20 S. K. Vashist and P. Vashist, *J. Sens.*, 2011, **2011**, 1–13.

21 S. Okur, P. Qin, A. Chandresh, C. Li, Z. Zhang, U. Lemmer and L. Heinke, *Angew. Chem., Int. Ed.*, 2021, **60**, 3566–3571.

22 O. M. Yaghi, M. O'Keeffe, N. W. Ockwig, H. K. Chae, M. Eddaoudi and J. Kim, *Nature*, 2003, **423**, 705–714.

23 I. Stassen, N. Burtch, A. Talin, P. Falcaro, M. Allendorf and R. Ameloot, *Chem. Soc. Rev.*, 2017, **46**, 3185–3241.

24 W. P. Lustig, S. Mukherjee, N. D. Rudd, A. V. Desai, J. Li and S. K. Ghosh, *Chem. Soc. Rev.*, 2017, **46**, 3242–3285.

25 T. Xu, P. Xu, D. Zheng, H. Yu and X. Li, *Anal. Chem.*, 2016, **88**, 12234–12240.

26 Y. Lv, P. Xu, H. Yu, J. Xu and X. Li, *Sens. Actuators, B*, 2018, **262**, 562–569.

27 J. Liu, E. Redel, S. Walheim, Z. Wang, V. Oberst, J. Liu, S. Heissler, A. Welle, M. Moosmann, T. Scherer, M. Bruns, H. Gliemann and C. Wöll, *Chem. Mater.*, 2015, **27**, 1991–1996.

28 M. G. Campbell and M. Dinca, *Sensors*, 2017, **17**, 1108.

29 M. G. Campbell, S. F. Liu, T. M. Swager and M. Dinca, *J. Am. Chem. Soc.*, 2015, **137**, 13780–13783.

30 J. A. Gustafson and C. E. Wilmer, *J. Phys. Chem. C*, 2017, **121**, 6033–6038.

31 J. A. Gustafson and C. E. Wilmer, *Sens. Actuators, B*, 2018, **267**, 483–493.

32 J. A. Gustafson and C. E. Wilmer, *ACS Sens.*, 2019, **4**, 1586–1593.

33 R. Sousa and C. M. Simon, *ACS Sens.*, 2020, **5**, 4035–4047.

34 A. Sturluson, R. Sousa, Y. Zhang, M. T. Huynh, C. Laird, A. H. P. York, C. Silsby, C. H. Chang and C. M. Simon, *ACS Appl. Mater. Interfaces*, 2020, **12**, 6546–6564.

35 I. Stassen, N. C. Burtch, A. A. Talin, P. Falcaro, M. D. Allendorf and R. Ameloot, *Chem. Soc. Rev.*, 2017, **46**, 3853.

36 L. J. Small, S. E. Henkelis, D. X. Rademacher, M. E. Schindelholz, J. L. Krumhansl, D. J. Vogel and T. M. Nenoff, *Adv. Funct. Mater.*, 2020, **30**, 8.

37 S. Kumar, Y. Pramudya, K. Müller, A. Chandresh, S. Dehm, S. Heidrich, A. Fediai, D. Parmar, D. Perera, M. Rommel, L. Heinke, W. Wenzel, C. Wöll and R. Krupke, *Adv. Mater.*, 2021, **33**, 2103316.

38 S. Okur, Z. Zhang, M. Sarheed, P. Nick, U. Lemmer and L. Heinke, *Sens. Actuators, B*, 2020, **306**, 127502.

39 A. Modrow, D. Zargarani, R. Herges and N. Stock, *Dalton Trans.*, 2012, **41**, 8690–8696.

40 S. Castellanos, F. Kapteijn and J. Gascon, *Crystengcomm*, 2016, **18**, 4006–4012.

41 Y. Jiang and L. Heinke, *Langmuir*, 2021, **37**, 2–15.

42 K. Müller, A. Knebel, F. Zhao, D. Bleger, J. Caro and L. Heinke, *Chem.–Eur. J.*, 2017, **23**, 5434–5438.

43 A. Knebel, L. Sundermann, A. Mohmeyer, I. Strauss, S. Friebe, P. Behrens and J. Caro, *Chem. Mater.*, 2017, **29**, 3111–3117.

44 J. Park, D. Q. Yuan, K. T. Pham, J. R. Li, A. Yakovenko and H. C. Zhou, *J. Am. Chem. Soc.*, 2012, **134**, 99–102.

45 O. Shekhah, H. Wang, S. Kowarik, F. Schreiber, M. Paulus, M. Tolan, C. Sternemann, F. Evers, D. Zacher, R. A. Fischer and C. Wöll, *J. Am. Chem. Soc.*, 2007, **129**, 15118–15119.

46 L. Heinke and C. Woll, *Adv. Mater.*, 2019, **31**, e1806324.

47 D. Bleger, J. Schwarz, A. M. Brouwer and S. Hecht, *J. Am. Chem. Soc.*, 2012, **134**, 20597–20600.

48 C. Knie, M. Utecht, F. Zhao, H. Kulla, S. Kovalenko, A. M. Brouwer, P. Saalfrank, S. Hecht and D. Bleger, *Chemistry*, 2014, **20**, 16492–16501.

49 K. Müller, J. Helfferich, F. Zhao, R. Verma, A. B. Kanj, V. Meded, D. Bleger, W. Wenzel and L. Heinke, *Adv. Mater.*, 2018, **30**, 1706551.

50 S. Güney and A. Atasoy, *Sens. Actuators, B*, 2012, **166–167**, 721–725.

51 S. Henke, R. Schmid, J. D. Grunwaldt and R. A. Fischer, *Chemistry*, 2010, **16**, 14296–14306.

52 S. Okur, M. Sarheed, R. Huber, Z. Zhang, L. Heinke, A. Kanbar, C. Wöll, P. Nick and U. Lemmer, *Chemosensors*, 2021, **9**, 31.

53 K. T. Tang, Y. S. Lin and J. M. Shyu, *Sensors*, 2010, **10**, 10467–10483.

54 U. Lall and A. Sharma, *Water Resour. Res.*, 1996, **32**, 679–693.

55 M. Jirina, *New fundamental technologies in data mining*, 2011, vol. 1, pp. 369–387.

56 P. E. Hart, D. G. Stork and R. O. Duda, *Pattern Classification*, Hoboken, Wiley, 2000.

57 A. B. Kanj, J. Burck, N. Vankova, C. Li, D. Mutruc, A. Chandresh, S. Hecht, T. Heine and L. Heinke, *J. Am. Chem. Soc.*, 2021, **143**, 7059–7068.

58 E. A. Meyer, R. K. Castellano and F. Diederich, *Angew. Chem., Int. Ed.*, 2003, **42**, 1210–1250.

59 K. Daze and F. Hof, Molecular Interaction and Recognition, in *Encyclopedia of Physical Organic Chemistry*, ed. Z. Wang, U. Wille, E. Juaristi, 2016, DOI: 10.1002/9781118468586.epoc3001.

60 G. Berger, P. Frangville and F. Meyer, *Chem. Commun.*, 2020, **56**, 4970–4981.

61 Z. Wang, S. Grosjean, S. Brase and L. Heinke, *ChemPhysChem*, 2015, **16**, 3779–3783.

62 H. B. Huang, H. Sato and T. Aida, *J. Am. Chem. Soc.*, 2017, **139**, 8784–8787.

63 J. Kärger, D. M. Ruthven and D. N. Theodorou, *Diffusion in Nanoporous Materials*, Wiley-VCH, 2012.

64 L. Heinke, Z. Gu and C. Wöll, *Nat. Commun.*, 2014, **5**, 4562.

65 L. Heinke, P. Kortunov, D. Tzoulaki and J. Kärger, *Phys. Rev. Lett.*, 2007, **99**, 228301.

66 Z. B. Wang, A. Knebel, S. Grosjean, D. Wagner, S. Brase, C. Woll, J. Caro and L. Heinke, *Nat. Commun.*, 2016, 7, 13872.

67 K. Tan, N. Nijem, P. Canepa, Q. Gong, J. Li, T. Thonhauser and Y. J. Chabal, *Chem. Mater.*, 2012, **24**, 3153–3167.

68 S. Castellanos, A. Goulet-Hanssens, F. L. Zhao, A. Dikhtiarenko, A. Pustovarenko, S. Hecht, J. Gascon, F. Kapteijn and D. Bleger, *Chem.–Eur. J.*, 2016, **22**, 746–752.

69 S. E. Henkelis, S. J. Percival, L. J. Small, D. X. Rademacher and T. M. Nenoff, *Membranes*, 2021, **11**, 176.

70 P. F. Shi, Y. C. Zhang, Z. P. Yu and S. S. Zhang, *Sci. Rep.*, 2017, 7, 7.

71 N. Ingle, P. Sayyad, G. Bodkhe, M. Mahadik, T. Al-Gahouari, S. Shirsat and M. D. Shirsat, *Appl. Phys. A: Mater. Sci. Process.*, 2020, **126**, 9.

72 Z. G. Gu, S. C. Chen, W. Q. Fu, Q. D. Zheng and J. Zhang, *ACS Appl. Mater. Interfaces*, 2017, **9**, 7259–7264.

73 J. Devkota, K. J. Kim, P. R. Ohodnicki, J. T. Culp, D. W. Greve and J. W. Lekse, *Nanoscale*, 2018, **10**, 8075–8087.

74 A. M. Ullman, C. G. Jones, F. P. Doty, V. Stavila, A. A. Talin and M. D. Allendorf, *ACS Appl. Mater. Interfaces*, 2018, **10**, 24201–24208.

75 A. Mirzaei, S. G. Leonardi and G. Neri, *Ceram. Int.*, 2016, **42**, 15119–15141.

76 S. Fanget, S. Hentz, P. Puget, J. Arcamone, M. Matheron, E. Colinet, P. Andreucci, L. Duraffourg, E. Myers and M. L. Roukes, *Sens. Actuators, B*, 2011, **160**, 804–821.

77 A. Oprea and U. Weimar, *Anal. Bioanal. Chem.*, 2019, **411**, 1761–1787.

78 M. Gutiérrez, C. Martín, B. E. Souza, M. Van der Auweraer, J. Hofkens and J.-C. Tan, *Applied Materials Today*, 2020, **21**, 100817.

79 P. Falcaro, R. Ricco, C. M. Doherty, K. Liang, A. J. Hill and M. J. Styles, *Chem. Soc. Rev.*, 2014, **43**, 5513–5560.

80 H. A. Schwartz, D. Schaniel and U. Ruschewitz, *Photochem. Photobiol. Sci.*, 2020, **19**, 1433–1441.

81 A. B. Kanj, A. Chandresh, A. Gerwien, S. Grosjean, S. Bräse, Y. Wang, H. Dube and L. Heinke, *Chem. Sci.*, 2020, **11**, 1404–1410.

82 H. A. Schwartz, H. Laurenzen, S. Kerschbaumer, M. Werker, S. Olthof, H. Kopacka, H. Huppertz, K. Meerholz and U. Ruschewitz, *Photochem. Photobiol. Sci.*, 2020, **19**, 1730–1740.

83 I. M. Walton, J. M. Cox, J. A. Coppin, C. M. Linderman, D. G. Patel and J. B. Benedict, *Chem. Commun.*, 2013, **49**, 8012–8014.

84 C. Eichler, A. Rázková, F. Müller, H. Kopacka, H. Huppertz, T. S. Hofer and H. A. Schwartz, *Chem. Mater.*, 2021, **33**, 3757–3766.

85 I. Stassen, I. Boldog, C. Steuwe, D. De Vos, M. Roeffaers, S. Furukawa and R. Ameloot, *Chem. Commun.*, 2017, **53**, 7222–7225.

86 Z. Wang, J. Liu, S. Grosjean, D. Wagner, W. Guo, Z. Gu, L. Heinke, H. Gliemann, S. Bräse and C. Wöll, *ChemNanoMat*, 2015, **1**, 338–345.

87 A. B. Kanj, J. Burck, S. Grosjean, S. Brase and L. Heinke, *Chem. Commun.*, 2019, **55**, 8776–8779.

88 K. Hoffmann, F. Marlow and J. Caro, *Adv. Mater.*, 1997, **9**, 567–570.

89 G. Das, T. Prakasam, M. A. Addicoat, S. K. Sharma, F. Rayaux, R. Mathew, M. Baias, R. Jagannathan, M. A. Olson and A. Trabolsi, *J. Am. Chem. Soc.*, 2019, **141**, 19078–19087.

90 Y. Zhu and W. Zhang, *Chem. Sci.*, 2014, **5**, 4957–4961.

91 N. K. Mal, M. Fujiwara, Y. Tanaka, T. Taguchi and M. Matsukata, *Chem. Mater.*, 2003, **15**, 3385–3394.

92 S. Angelos, E. Choi, F. Vogtle, L. De Cola and J. I. Zink, *J. Phys. Chem. C*, 2007, **111**, 6589–6592.

93 Z. L. Chu, Y. X. Han, T. Bian, S. De, P. Kral and R. Klajn, *J. Am. Chem. Soc.*, 2019, **141**, 1949–1960.

94 S. Das, P. Ranjan, P. S. Maiti, G. Singh, G. Leitus and R. Klajn, *Adv. Mater.*, 2013, **25**, 422–426.

95 A. Oprea and U. Weimar, *Anal. Bioanal. Chem.*, 2020, **412**, 6707–6776.

96 K. Sahner, G. Hagen, D. Schonauer, S. Reiss and R. Moos, *Solid State Ionics*, 2008, **179**, 2416–2423.